Geochemical Perspectives Letters

Origins of the pervasive luminescence in modern stromatolites

J. Debrie, J-P. Saint Martin, D. Prêt, F. Lam, K. Medjoubi, A. Somogyi, K. Benzerara

Supplementary Information

The Supplementary Information includes:

- Materials and Methods
- Figures S-1 to S-3
- Table S-1
- Supplementary Information References

Materials and methods

Geological setting

The geological context has been thoroughly detailed in Saint Martin and Saint Martin (2015) and in Debrie *et al.*, (2022).

Sample preparation

Petrographic thin sections were prepared for light electron and confocal microscopies. First, the stromatolite samples were cut in half using a circular saw. One half was embedded in a polyester resin (GBS1, Aeri SAS) under vacuum, then sawn and glued on a glass slide with Araldite (HUNTSMAN). Finally, it was thinned by raw polishing down to 30 µm in thickness and latter polished with alumina suspension (0.1 µm grain size) to remove surface roughness.

Macroscope images

A petrographic thin section measuring 30 µm in thickness was fully imaged in transmitted (brightfield mode) and epifluorescence light at large scale using a stereo macro-apotome Zeiss Axio Zoom V16 equipped with a motorized stage. The two objectives used were a 1x with a numerical aperture (NA) of 0.25 and a 2.3x with a NA of 0.57. The excitation source was a fluorescent lamp (HXP 200) and we used adapted block filters to image the different channels: a GFP filter (excitation: 450/50, emission: 510/50 nm) and a CY5 filter (excitation: 640/30, emission: 690/50) for the green and magenta channels respectively.

Scanning electron microscopy

Petrographic thin sections were carbon-coated to make their surface conductive for electrons. They were fixed to an aluminium holder using copper tape. Petrographic thin sections were observed by scanning electron microscopy (SEM) at IMPMC, using a SEM-FEG Zeiss Crossbeam Neon40 EsB equipped with the Atlas5 module. A high resolution centimetric mosaic (3.46 × 4.14 cm^2, 231 000 × 276 000 pixels, pixel size of 150 nm), covering most of one stromatolite sample was built from 77 x 92 tiles, using an acceleration voltage of 15 kV, a working distance of 12 mm and a dwell time of 3.0 µs per pixel.

Confocal laser scanning microscopy (CLSM)

CLSM analyses were performed on thin slides of c.a. 30 µm in thickness, prepared with the non-fluorescent polyester resin (GBS1, Aeri SAS). CLSM samples were examined using a Zeiss LSM 710 confocal laser scanning microscope (IMPMC) mounted on an AxioImager z2 with a lateral resolution of 0.4 µm. The Zeiss LSM 710 was equipped with a 405 nm laser diode and multiline argon (458, 488 and 514 nm), helium-neon-green (543 nm) and helium-neon-red (633 nm) lasers. Hyperspectral emission data were measured in the lambda mode between 415 and 730 nm, over 32 channels with a spectral resolution of 10 nm. Luminescence was excited simultaneously at 405, 488 and 633 nm, with laser/diode intensities at 3, 2.5 and 0.5%, respectively. A bright field image was also acquired with the T-PMT detector. An MBS 405/488/543/633 filter was used in the excitation light path. Images were acquired with a 10x or 20x objective and with a scan time up to 1.1 s / pixel. and total acquisition times c.a. 20 minutes.

Hyperspectral data analysis

Preliminary processes

Hyperspectral data acquired on the confocal microscope were initially composed of 32 z-stacked emission images (the dataset used in Figures 3, S-1 and S-2 can be downloaded at https://doi.org/10.5281/zenodo.14998864 and can be read using the opensource FIJI software). Because of the MBS filter, the images obtained at 488, 537, 546 and 634 nm show no fluorescence signal and were deleted. Consequently, the hyperspectral data is a combination of 28 images collected for 28 emission wavelengths from 430 to 720 nm with a spectral step of 10 nm.

Image processing for the study of fluorescence signal distribution

Each of the scanned pixels corresponds to a fluorescence spectrum that has not been assimilated in a straightforward way to a pure component. As each of the fluorescent spectra has a varying contribution in the blue-green, yellow and red visible regions of light, it seems that the fluorescent spectra are the result of a mixture of compounds rather than a single compound. Contributions C1, C2 and C3, corresponding to the green, yellow and red regions respectively, were defined as follows:

C1 = sum of the channels 1 to 11 – stack image between 430 and 537 nm
C2 = sum of the channels 12 to 19 – stack image between 556 and 624 nm
C3 = sum of the channels 20 to 28 – stack image between 644 and 722 nm

Next, all the pixels were projected into a ternary diagram. The ternary diagram is supported by “green”, “yellow” and “red” poles (C1, C2 and C3 respectively), allowing the dispersion of pixels between these three poles to be mapped. The µPhaseMap software (Prêt *et al.*, 2010a, b; Debrie *et al.*, 2022) has often been used to process elemental chemistry hyperspectral data. Here, we used it to process the fluorescence emission hyperspectral data and C1, C2 and C3 were used as input parameters. Further details about this approach are provided in Prêt *et al.*, (2010a, b).

Pixel selection on ternary diagrams

The pixels plotted in the ternary diagram were grouped into three different sets surrounded by coloured polygons drawn by the software user: 1) a group of pixels (outlined by a green polygon) encompassing almost all the pixels, located along the C1”green”-C2”yellow” axis and corresponding to the pixels with a varying contribution between the green and the yellow; 2) a group of pixels (outlined by a pink polygon) in a mixture tending towards the C3 ”red” pole, and 3) a third group of pixels (outlined by a yellow polygon) spreading between the first (C1-C2) group and a pole located closer to C3. The selected pixels were then backprojected into the fluorescence stack image using the same colour as that chosen for the polygon.

Determination of the fluorescence signatures

From each polygon, a small group of pixels, assumed to be the most representative set of pixels from the selected cluster, were manually extracted (marked by a square on ternary scatterplots). The square position for the green cluster is located at the maximum pixel frequency, almost corresponding to the cluster centroid. For the yellow and red clusters, mixture

lines towards pure endmembers are detected but pixel frequencies decrease (from light to dark blue) when going towards the end of the mixture lines. This pattern shows an intricated mixture of signals and that there is no large enough area with pure yellow or pure red spectra (Prêt *et al.*, 2010a, b). As a result, no Gaussian-like distribution of pixel frequencies is observed for these clusters, complicating a proper centroid determination. When dealing with intense mixing without Gaussian distribution, it has been demonstrated that outlying mixtures and clusters on ternary or binary scatterplots by well-chosen user-controlled polygons is more satisfying than processing simple K-means or state of the art clustering algorithms (Lanari and Tedeschi, 2025). Then, these "purest" pixels were backprojected onto the stack image, which was further converted into a binary mask. A fluorescence spectrum was obtained by integrating the measured fluorescence intensity over the selected area. Finally, the highest intensity of each of the three measured fluorescence spectra was normalised to 1.

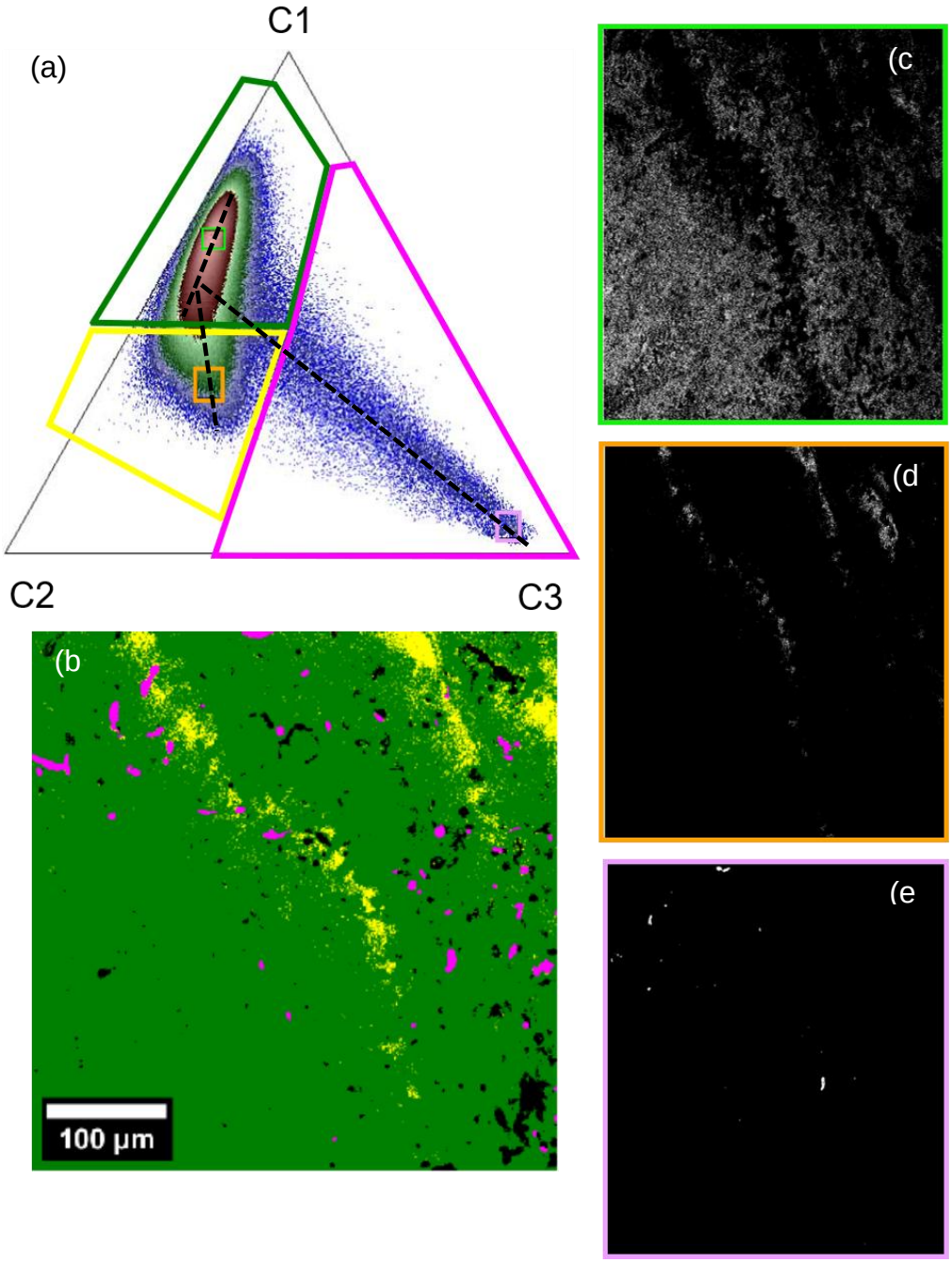

Figure S-1 Methodology of segmentation. All pixels of the hyperspectral CLSM images are plotted in a C1-C2-C3 ternary diagram (a), where C1 (430 to 537 nm), C2 (556 to 624 nm) and C3 (644 to 722 nm) correspond to the green, yellow and red spectral relative contributions to the emission spectrum of each spectrum. The local frequency of pixels on this scatterplot is encoded by using a logarithmic 3Bands color scale for which blue hues are associated with few-pixel densities, while red reflects thousands of pixels. The coloured polygons outline the selected pixels for each cluster backprojected in the fluorescence stack image (b). The smaller squares indicate the purest pixels selected to extract measured emission spectra representative of the three spectral components (see spectra in Figure 3 in the main manuscript). (c, d & e). Green and pink boxes outline the highest density pixel areas at extremities of mixing lines, indicated by dashed lines. The deviation/curvation at the bottom of the C1-C2 pixel cloud towards the middle of the C2-C3 axis (see dashed line) suggests the presence of a third, subtler component outline by the orange box. (c), (d) and (e): Masks corresponding to the intensity maps associated with the pixels surrounded by the green, orange and pink squares, from which the fluorescence spectra are extracted.

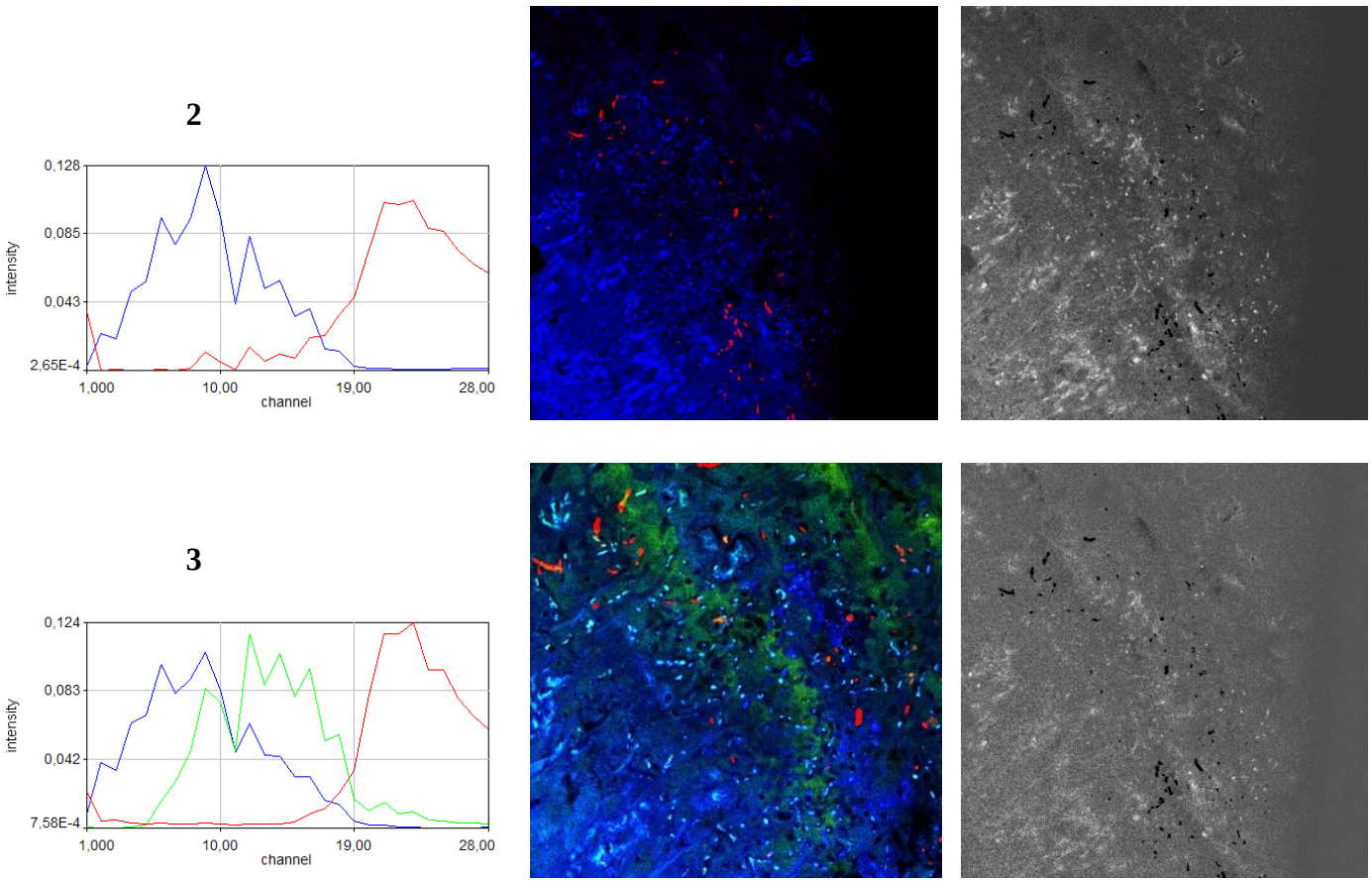

Figure S-2 Multivariate statistical analysis of the hyperspectral dataset (same as used in Figure 3) using non-negative matrix factorization (NNMF). The NNMF Spectral Unmixing JRU v1 plugin from Jay Unruh at Stowers Institute for Medical Research (Kansas City, MO; Neher *et al.*, 2009) was used with 50 iterations. Output endmember spectra, composite image showing their distribution and total residue (obtained by flattening the residual stack provided by FIJI) obtained by using two components (top row) or three components (bottom row). The appearance of distinct spatial features (in green) and a decrease of the total residue suggest that it was appropriate to use three instead of two components. On the contrary to the ternary scatterplot approach, the output spectra are 'theoretical" and not real, measured ones.

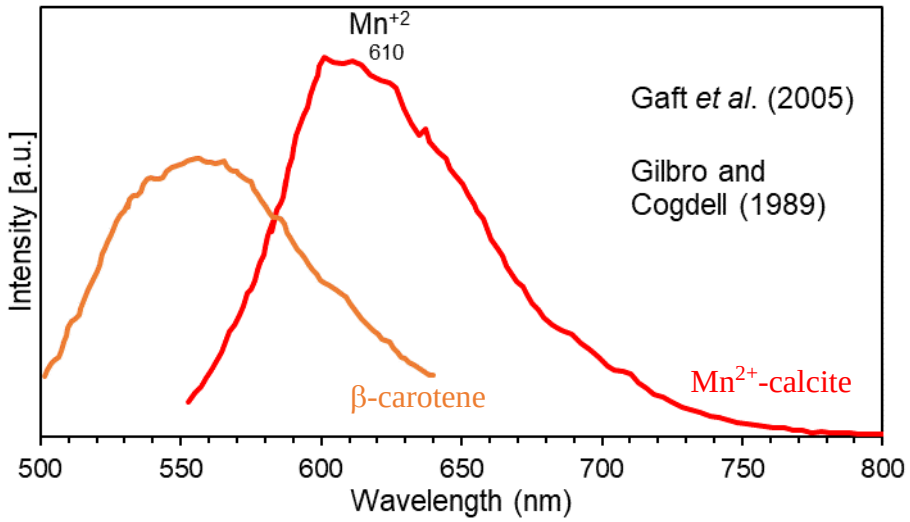

Figure S-3 Reference fluorescence spectra of β-carotene and Mn^{2+}-containing calcite. In orange, fluorescence spectrum of β-carotene modified from Gilbro and Cogdell (1989). In red, fluorescence spectrum of a Mn^{2+}-containing calcite from Canada modified from Gaft *et al*., (2005). For calcite, the spectrum was obtained with an excitation at 532 nm.

Table S-1 Major element compositions of microbialites from Mari Ermi lagoons obtained by bulk chemical analyses (LOI = loss of ignition). Table from Debrie *et al*., (2022). The first two lines provide the oxide wt. % (e.g., SiO_2 wt. %). The two last lines provide the conversion into elemental weight % (e.g., Si wt. %).

Sample	SiO_2 (wt. %)	Al_2O_3 (wt. %)	Fe_2O_3 (wt. %)	MgO (wt. %)	CaO (wt. %)	Na_2O (wt. %)	K_2O (wt. %)	MnO (wt. %)	TiO_2 (wt. %)	Mg/Ca (atom)	LOI (wt. %)	Total
SAR16-MES-1	2.72	0.46	0.27	4.8	43.4	0.91	0.12	0.04	0.025	0.19	46.18	99.0
	± 0.2	± 0.09	± 0.05	± 0.5	± 0.9	± 0.09	± 0.04	± 0.04	± 0.006	± 0.02		
SAR16-MEN-1	2.24	0.5	0.46	5.2	42.6	0.9	0.19	0.0869	0.024	0.205	46.29	98.7
	± 0.2	± 0.1	± 0.09	± 0.1	± 0.8	± 0.1	± 0.04	± 0.04	± 0.008	± 0.05		
	Si (wt. %)	Al (wt. %)	Fe (wt. %)	Mg (wt. %)	Ca (wt. %)	Na (wt. %)	K (wt.)	Mn (wt. %)	Ti (wt. %)	Mg/Ca (atom)		
SAR16-MES-1	1.2	0.25	0.21	2.9	30.8	0.7	0.12	0.03	0.015	0.16		
SAR16-MEN-1	1	0.28	0.36	3.15	30.3	0.7	0.156	0.067	0.0144	0.17		

Supplementary Information References

Debrie, J., Prêt, D., Menguy, N., Estève, I., Sans-Jofre, P., Saint Martin, J.P., Benzerara, K. (2022) Mapping mineralogical heterogeneities at the nm-scale by scanning electron microscopy in modern Sardinian stromatolites: Deciphering the origin of their laminations. *Chemical Geology* 609, 121059. https://doi.org/10.1016/j.chemgeo.2022.121059

Gaft, M., Reisfeld, R., Panczer, G. (2005) *Luminescence spectroscopy of Minerals and Materials*. Berlin Heidelberg.

Gillbro, T., Cogdell, R.J. (1989) Carotenoid fluorescence. *Chemical Physics Letters* 158, 312-316. https://doi.org/10.1016/0009-2614(89)87342-7

Lanari, P., Tedeschi, M. (2025) Chemical map classification in XMapTools. *Applied Computing and Geosciences* 25, 100230. https://doi.org/10.1016/j.acags.2025.100230

Neher, R.A., Mitkovski, M., Kirchhoff, F., Neher, E., Theis, F.J., Zeug, A. (2009) Blind source separation techniques for the decomposition of multiply labeled fluorescence images. *Biophysical Journal* 96, 3791-800. https://doi.org/10.1016/j.bpj.2008.10.068

Prêt, D., Sammartino, S., Beaufort, D., Meunier, A., Fialin, M., Michot, L.J. (2010a) A new method for quantitative petrography based on image processing of chemical element maps: Part I. Mineral mapping applied to compacted bentonites. *American Mineralogist* 95, 1379-1388. https://doi.org/10.2138/am.2010.3431

Prêt, D., Sammartino, S., Beaufort, D., Fialin, M., Sardini, P., Cosenza, P., Meunier, A. (2010b) A new method for quantitative petrography based on image processing of chemical element maps: Part II. Semi-quantitative porosity maps superimposed on mineral maps. *American Mineralogist* 95, 1389-1398. https://doi.org/10.2138/am.2010.3433

Saint Martin, J.P., Saint Martin, S. (2015) Discovery of calcareous microbialites in coastal ponds of western Sardinia (Italy). *Geo-Eco-Marina*, 35-53.